Publications of the Korean Astronomical Society
32: 245 ∼ 249, 2017 March

pISSN 1225-1534
eISSN 2287-6936
https://doi.org/10.5303/PKAS.2017.32.1.245

PROPERTIES OF DUST OBSCURED GALAXIES IN THE NEP-DEEP FIELD

Nagisa Oi[1], Hideo Matsuhara[1,8], Chris Pearson[2,3,4], Veronique Buat[5], Denis Burgarella[5], Matt Malkan[6], Takamitsu Miyaji[7], and AKARI-NEP team[1]

[1]Department of Infrared Astrophysics Institute of Space and Astronautical Science, Japan Aerospace Exploration Agency, 3-1-1 Yoshinodai, Chuo-ku, Sagamihara 252-5210 Japan
[2]Department of Physical Sciences, The Open University, Milton Keynes, MK7 6AA, UK
[3]Rutherford Appleton Laboratory Oxon, OX11 0QX, UK
[4]Oxford Astrophysics, Denys Wilkinson Building, University of Oxford, Keble Rd, Oxford OX1 3RH, UK
[5]Aix-Marseille Université, CNRS, LAM (Laboratoire d'Astrophysique de Marseille) UMR7326, 13388, Marseille, France
[6]Department of Physics and Astronomy, UCLA, Los Angeles, CA, 90095-1547, USA
[7]Universidad Nacional Autónoma de México
[8]Department of Space and Astronautical Science, The Graduate University for Advanced Studies, Japan

E-mail: nagisaoi@ir.isas.jaxa.jp

(Received July 23, 2015; Revised October 20, 2016; Accepted October 20, 2016)

ABSTRACT

We selected 47 DOGs at $z \sim 1.5$ using optical R (or r'), AKARI 18 μm, and 24 μm color in the AKARI North Ecliptic Pole (NEP) Deep survey field. Using the colors among 3, 4, 7, and 9μm, we classified them into 3 groups; bump DOGs (23 sources), power-law DOGs (16 sources), and unknown DOGs (8 sources). We built spectral energy distributions (SEDs) with optical to far-infrared photometric data and investigated their properties using SED fitting method. We found that AGN activity such as a AGN contribution to the infrared luminosity and a Chandra detection rate for bump and power-law DOGs are significantly different, while stellar component properties like a stellar mass and a star-formation rate are similar to each other. A specific star-formation rate range of power-law DOGs is slightly higher than that of bump DOGs with wide overlap. Herschel/PACS detection rates are almost the same between bump and power-law DOGs. On the other hand SPIRE detection rates show large differences between bump and power-law DOGs. These results might be explained by differences in dust temperatures. Both groups of DOGs host hot and/or warm dust ($\sim$ 50 Kelvin), and many bump DOGs contain cooler dust ($\lesssim$ 30 Kelvin).

Key words: Infrared galaxies, Dusty galaxies, High redshift galaxies, AKARI, Deep survey

1. INTRODUCTION

Infrared luminous galaxies ($L_{IR} > 10^{11} L_{\odot}$) dominate the bright end of the bolometric luminosity function of galaxies in the local universe (Soifer et al., 1986). Their role in the history of galaxy evolution is not yet understood, but it is likely that their vast infrared luminosities (L_{IR}) are the product of an extremely active phase during which these systems form stars and/or grow their central black holes at a rapid rate in the region hidden by dust. Studies of the extragalactic background have suggested at least one third (or half) of the luminous energy generated by stars has been reprocessed into the infrared (IR) by dust (Lagache et al., 1999) and that the contribution of infrared luminous sources to the cosmic infrared luminosity density increases with redshift, especially at $z > 1$ (Goto et al., 2010). Therefore, in order to understand the cosmic star formation history, studying infrared luminous galaxies is inevitable.

Dey et al. (2008) used *Spitzer* to select optically-faint ultra-luminous infrared galaxies using a very sim-

ple optical and mid-IR color ($R - [24] > 14$ Vega magnitudes), called dust-obscured galaxies (DOGs), lying at $z \sim 2$. DOGs can be divided into two classes according to the nature of their mid-IR spectral energy distributions (SEDs), one is galaxies showing the rest frame 1.6μm bump in their SEDs indicative of the photospheres of late type stars (bump DOGs), and the other is those dominated by a power law in the near to mid-IR (power-law DOGs). Hence, DOGs could be keys to understanding activity (star-formation / AGN) hidden by dust at high-z. However, *Spitzer* lacks filters between 8 and 24μm (the critical gap between the Infrared Array Camera (IRAC) and the Multiband Imaging Photometer (MIPS), excluding the tiny IRS peak up array at 16μm), although SEDs of star-formation dominated DOGs and of AGN dominated DOGs are significantly different at mid-IR wavelengths. In contrast, AKARI infrared satellite/InfraRed Camera (IRC) covers 2 – 24μm continuously without any large wavelength gaps. In this work, we study the properties of AKARI / IRC detected DOGs using the continuous mid-IR AKARI data with multi-wavelength photometric data (from X-ray to far-IR), and fitting the SEDs from the optical to the far-IR.

2. SAMPLE SELECTION

2.1. Imaging Data

AKARI carried out a deep survey program in the direction of north ecliptic pole (NEP), the so-called NEP-Deep survey (Matsuhara et al., 2006), extensively observed in all the available IRC 9 bands ($N2$, $N3$, $N4$, $S7$, $S9W$, $S11$, $L15$, $L18W$, and $L24$). In this survey, 11349 mid-IR sources are detected (Murata et al., 2013). The field is a unique region because many astronomical satellites accumulated many exposures thanks to the nature of its position on the sky, and ground based telescopes deeply observed the region. The Subaru/S-cam deep images (B, V, R, i, z) covers 40 % of the NEP-Deep field. The CFHT/MegaCam (u^*, $g^{'}$, $r^{'}$, $i^{'}$, $z^{'}$) and WIRCam (Y, J, $K_{\rm s}$) images are not as deep as S-cam images but cover almost the entire field of NEP-Deep field. By combining these data with Herschel/PACS and SPIRE data, we can build optical to far-IR SEDs.

2.2. Sample Selection

Our sample is selected from the 0.5 deg^2 region of the NEP-Deep field with S-cam R-band and CFHT MegaCam $r^{'}$-band. The criteria for selecting DOGs are as follows:

$$Scam\ R - (L18W\ or\ L24) > 7.5\ (AB)\ \mathrm{mag} \quad (1)$$

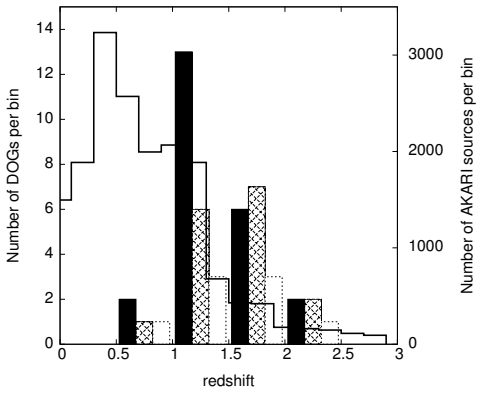

Figure 1. The redshift distributions of bump DOGs (solid bars), power-law DOGs (shadowed bars), and unknown DOGs (open bars). The redshift distribution of all AKARI-detected sources is overplotted as a solid line.

or

$$MegaCam\ r^{'} - (L18W\ or\ L24) > 7.5\ (AB)\ \mathrm{mag} \quad (2)$$
$$\&\ MegaCam\ r^{'} < 25.9\ (AB)\ \mathrm{mag}. \quad (3)$$

Since the $L24$ filter is not as sensitive as the $L18W$ and the $L18W$ filter covers almost full range of the $L24$ filter range, we used not only $L24$ but also $L18W$ filter for the DOG selection. Since the S-cam data are deeper than MegaCam data, we used the criterion (1) in the Scam field, while outside of the S-cam field we used the criterion (2). The MegaCam data are not deep enough to detect most AKARI DOGs, especially those detected at $> 5\sigma$ at $L18W$, so we also applied criterion (3). Moreover, we removed AKARI sources blended with nearby sources to prevent fake DOGs in our target list. Finally, there are 110 sources satisfying these criteria in the NEP-Deep field.

To measure photometric redshifts (z_p) of the DOGs, we used a SED fitting code *Le Phare* (Ilbert et al., 2006). For the DOGs located in the S-cam field, we used S-cam 5 bands, MegaCam $u^*, g^{'}, r^{'}$, and WIRCam $Y, J, K_{\rm s}$ bands for z_p calculation, while DOGs located outside of the S-cam filed, we adopted z_p calculated by Oi et al. (2014).

In order to measure reliable physical parameters of DOGs, in this work we added more rigorous criteria for selecting DOGs and created secure subsamples. First, we selected secure targets with $0.5 < z_p < 3$, because during the z_p calculation the SED fitting code sometimes misidentifies the Balmer break and the Lyman break causing miscalculation of z_p between low-z ($z < 0.5$) and high-z ($z \sim 3-4$). 47 secure DOGs are selected. Next, we classified the DOGs into star-formation DOGs (bump DOGs) and AGN-like DOGs (power-law

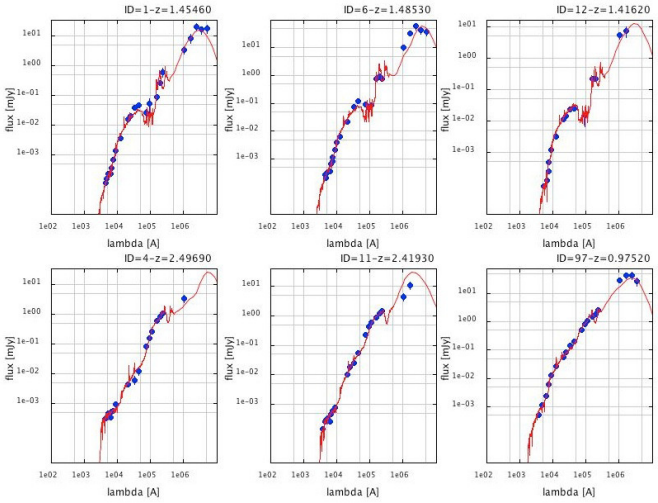

Figure 2. Examples of observed SEDs classified as bump DOGs (top) and power-law DOGs (bottom) with the best models using CIGALE (red lines).

DOGs) using $N3$, $N4$, $S7$, and $S9W$. Bump DOGs are expected to show the stellar-bump at rest-frame 1.6μm. On the other hand power-law DOGs are expected to have monotonically increasing red spectra in the mid-IR. We therefore classified into bump DOGs with the following criteria of (4) – (6), and into power-law DOGs with criteria of (7) and (8). If a source does not meet both bump and power-law DOG criteria, then it is classified as an unknown DOG.

$$f_{N3} \leq f_{N4} \ \& \ f_{N4} \geq f_{S7} \quad (4)$$
$$f_{N3} \leq f_{N4} \ \& \ f_{N4} \geq f_{S9W} \quad (5)$$
$$f_{N4} \leq f_{S7} \ \& \ f_{S7} \geq f_{S9W} \quad (6)$$

$$f_{N3} \leq f_{N4} \leq f_{S7} \leq f_{S9W} \quad (7)$$
$$f_{N4} \leq f_{S7} \leq f_{S9W}, \quad (8)$$

where f_X represents a X filter flux. In total, the number of sources classified as bump, power-law, and unknown DOGs are 23, 16, and 8, respectively. 5 out of 16 power-law DOGs (>30 %) are detected by Chandra X-ray data, while only one bump DOG out of 23 sources (< 5 %) is detected.

Redshift distributions of bump DOGs, power-law DOGs, and unknown DOGs are shown in Figure 1, with the distribution of AKARI sources in the NEP-Deep survey. The figure shows that the AKARI DOGs are distributed at around $z \sim 1.5$ and these distributions of the bump and power-law DOGs are similar to each other.

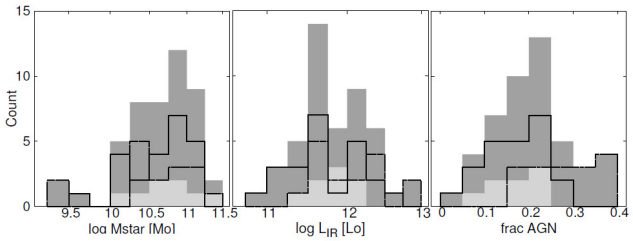

Figure 3. Distributions of stellar mass (left), infrared luminosity (middle), and AGN fraction (right) estimated by CIGALE. Thick solid and thin dotted lines represent bump and power-law DOGs, respectively. Dark-filled gray and light-gray bars show all 47 DOGs and unknown DOGs, respectively.

3. SED FITTING

The SED fitting is performed with the CIGALE[1] code (Code Investigating GALaxy Emission) developed in Fortran by Noll et al. (2009). This is a physically-motivated code that derives properties of galaxies by fitting their ultraviolet(UV)-to-far-IR SEDs. CIGALE combines a UV-optical stellar SED and an IR dust emission component, and fully conserves the energetic balance between the dust absorbed stellar emission and its re-emission in the IR. CIGALE can select among two single stellar population libraries and several IR models/templates and performs a Bayesian analysis to estimate parameters. An AGN component can also be added to estimate the AGN fraction (AGN contribution to the L_{IR}).

We assumed two stellar populations, a recent stellar population (age: 10 – 100 Myr) with a constant SFR on top of an older stellar population (age: 0.1 – 3 Gyr) created with an exponentially declining SFR ($\propto e^{-\tau}$). The stellar population synthesis models of Maraston (2005), the Kroupa initial mass function (Kroupa 2001) and a metallicity of 1.0 $Z_\odot$ are assumed. The extinction curve of Calzetti et al. (2000) is also assumed. We fixed redshifts determined by *Le Phare*. The IR dust emission is fitted using the Dale & Helou (2002) library, and Fritz et al. (2006) library is used as AGN models. Examples of SEDs with the best models selected by CIGALE are shown in Figure 2.

[1] http://cigale.lam.fr

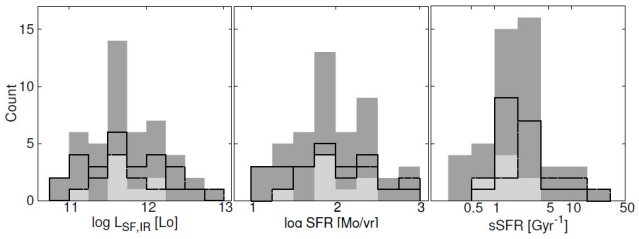

Figure 4. Distributions of infrared luminosity emitted from star formation (left), SFR (middle), and sSFR (right). Indices are the same as Fig. 3.

4. PROPERTIES OF BUMP AND POWER-LAW DOGs

4.1. Stellar and AGN properties

Properties of our DOG samples measured from the SED fitting are shown in Figure 3. The stellar mass ranges for bump DOGs and power-law DOGs are both $10^{9.5-11.5} M_{\odot}$, and these distributions are very similar to each other. On the other hand, the distribution of L_{IR} of power-law DOGs is slightly shifted to higher values compared with bump DOGs. However, the L_{IR} includes the emission from not only star-formation but also from AGN. The AGN fractions of L_{IR} are shown in the right panel of Figure 3. The fraction range of power-law DOGs is significantly higher (15% – 40%) than that of bump DOGs (0% – 30%). To compare the stellar component properties between bump and power-law DOGs, we removed the effect of AGN emission and estimated infrared luminosity from star-formation ($L_{IR,SF}$), star-formation rate (SFR), and specific SFR (sSFR) with these equations,

$$L_{IR,SF} = L_{IR} \times (1 - f_{AGN}) \quad (9)$$

$$SFR = 1.7 \times 10^{-10} \times L_{IR,SF} \quad (10)$$

$$sSFR = SFR/M_{star}. \quad (11)$$

The distributions of those physical parameters are shown in Figure 4. The range of $L_{IR,SF}$ of power-law DOGs is quite similar to that of bump DOGs. The SFR measured from the $L_{IR,SF}$ is 10 – 1000 $M_{\odot}$ yr^{-1} for both of bump and power-law DOGs. The distribution of sSFR for power-law DOGs is slightly larger (0.8 – 30 Gyr^{-1}) compared with that for bump DOGs (0.4 – 10 Gyr^{-1}) but those ranges overlap widely. All stellar component properties (M_{star}, SFR, sSFR) are similar between bump-DOGs and power-law DOGs suggesting that bump and power-law DOG are similar populations, and only AGN activities are significantly different.

Although SFRs are not yet well known in *Spitzer*-detected $z \sim 2$ DOGs, early evidence indicates that bump DOGs may have SFRs $\sim 1000\ M_{\odot}$ yr $^{-1}$ (Lonsdale et al., 2009; Kovács et al., 2010), whereas power-law DOGs may have much lower SFRs (e.g., $\sim 100\ M_{\odot}$ yr $^{-1}$; Melbourne et al., 2011). Also the sSFRs for $z \sim 2$ DOGs are $\sim$ 1 – 10 Gyr^{-1} (Bussmann et al., 2012). Comparing our $z \sim 1.5$ DOGs with the $z \sim 2$ DOGs, the $z \sim 1.5$ bump DOGs have lower SFR but similar sSFR to $z \sim 2$ bump DOGs, whereas the $z \sim 1.5$ power-law DOGs have similar SFR but similar or slightly higher sSFR.

4.2. Properties of Dust Temperature

Figure 5 shows histograms of detection rates for both bump and power-law DOGs. The detection rates at the Herschel/PACS bands are similar to each other ($\sim$ 75% of sources are detected at 100μm band and $\sim$ 50% of sources are detected at 160μm band). On the other hand, the power-law DOGs are less likely to be detected in the SPIRE bands than the bump DOGs: only 30% of the power-law DOGs are detected, while $\sim$ 50% of the bump DOGs are detected. Even the redshift distributions of bump DOGs and power-law DOGs are not significantly different (Figure 2) and L_{IR} of power-law DOGs are slightly higher compared with that of bump DOGs (the middle panel of Figure 3).

Because the DOGs are selected to be luminous at 18μm or 24μm, they are likely to host significant amounts of hot and warm dust. Assuming the dust emission follows a simple blackbody, the dust emission peak of DOGs at $z \sim 1.5$ with temperature of 45 – 75 K (= the emission peak at rest frame 40 – 65 μm) is at PACS wavelengths. In contrast, dust emission peaks with temperatures of 15 – 30 K are redshifted into SPIRE wavelengths. The result might suggest that both bump DOGs and power-law DOGs host warm ($\sim$ 50 Kelvin) dust, while bump DOGs also contain cooler ($\lesssim$ 30 Kelvin) dust.

ACKNOWLEDGMENTS

We acknowledge the support by the Japan Society for the Promotion of Science (JSPS; grant number 23244040).

REFERENCES

Bussmann, R. S., Dey, A., Armus, L., et al., 2012, The Star Formation Histories of z 2 Dust-obscured Galaxies and Submillimeter-selected Galaxies, ApJ, 744, 150

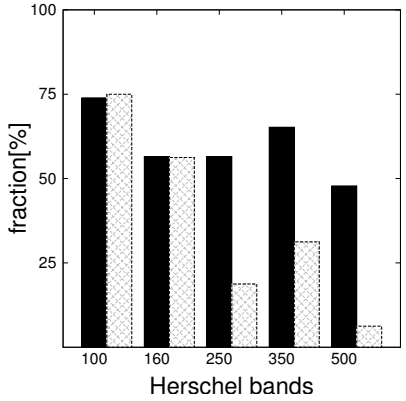

Figure 5. Detection rates at Herschel/PACS and SPIRE wavelengths. Solid bars represent the bump DOGs and shadowed ones show the power-law DOGs.

Calzetti, D., Armus, L., Bohlin, R. C., et al., 2000, The Dust Content and Opacity of Actively Star-forming Galaxies, ApJ, 533, 682

Dale, D. A. & Helou, G., 2002, The Infrared Spectral Energy Distribution of Normal Star-forming Galaxies: Calibration at Far-Infrared and Submillimeter Wavelengths, ApJ,, 576, 159

Dey, A., Soifer, B. T., Desai, V., et al., 2008, A Significant Population of Very Luminous Dust-Obscured Galaxies at Redshift $z \sim 2$, ApJ, 677, 943

Fritz, J., 2006, Revisiting the infrared spectra of active galactic nuclei with a new torus emission model, MNRAS, 366, 767

Goto, T., Takagi, T., Matsuhara, H., et al., 2010, Evolution of infrared luminosity functions of galaxies in the AKARI NEP-deep field. Revealing the cosmic star formation history hidden by dust, A&A, 514, A6

Ilbert, O., Arnouts, S., McCracken, H. J., et al., 2006, Accurate photometric redshifts for the CFHT legacy survey calibrated using the VIMOS VLT deep survey, A&A, 457, 841

Kovács, A., Omont, A., Beelen, A., et al., 2010, Far-infrared Properties of Spitzer-selected Luminous Starbursts, ApJ, 717, 29

Kroupa, P., 2001, On the variation of the initial mass function, MNRAS, 322, 231

Lagache, G., Abergel, A., Boulanger, F., Désert, F. X., & Puget, J. -L., 1999, First detection of the warm ionised medium dust emission. Implication for the cosmic far-infrared background, A&A, 344, 322

Lonsdale, C. J., Polletta, M. d. C., Omont, A., et al., 2009, MAMBO 1.2 mm Observations of Luminous Starbursts at z 2 in the SWIRE Fields, ApJ, 692, 422

Maraston, C., 2005, Evolutionary population synthesis: models, analysis of the ingredients and application to high-z galaxies, MNRAS, 362, 799

Matsuhara, H., Wada, T., Matsuura, S., et al., 2006, Deep Extragalactic Surveys around the Ecliptic Poles with AKARI (ASTRO-F), PASJ, 58, 673

Melbourne, J., Peng, C. Y., Soifer, B. T., et al., 2011, The Black Hole Masses and Star Formation Rates of $z > 1$ Dust Obscured Galaxies: Results from Keck OSIRIS Integral Field Spectroscopy, AJ, 141, 141

Murata, K., Matsuhara, H., Wada, T., et al., 2013, AKARI North Ecliptic Pole Deep Survey. Revision of the catalogue via a new image analysis, A&A, 559A, 132

Noll, S., Burgarella, D., Giovannoli, E., et al., 2009, Analysis of galaxy spectral energy distributions from far-UV to far-IR with CIGALE: studying a SINGS test sample, A&A, 507, 1793

Oi, N., Matsuhara, H., Murata, K., et al., 2014, Optical - near-infrared catalog for the AKARI north ecliptic pole Deep field, A&A, 566A, 60

Soifer, B. T., Sanders, D. B., Neugebauer, G., et al., 1986, The luminosity function and space density of the most luminous galaxies in the IRAS survey, ApJ, 303, L41